arXiv:1612.08151v1 [cond-mat.soft] 24 Dec 2016

Colloidal transport by active filaments

Raj Kumar Manna,[1] P. B. Sunil Kumar,[1] and R. Adhikari[2]

[1] *Department of Physics, Indian Institute of Technology Madras, Chennai 600036, India*
[2] *The Institute of Mathematical Sciences-HBNI, CIT Campus, Chennai 600113, India*

Enhanced colloidal transport beyond the limit imposed by diffusion is usually achieved through external fields. Here, we demonstrate the ballistic transport of a colloidal sphere using internal sources of energy provided by an attached active filament. The latter is modeled as a chain of chemo-mechanically active beads connected by potentials that enforce semi-flexibility and self-avoidance. The fluid flow produced by the active beads and the forces they mediate are explicitly taken into account in the overdamped equations of motion describing the colloid-filament assembly. The speed and efficiency of transport depend on the dynamical conformational states of the filament. We characterize these states using filament writhe as an order parameter and identify ones yielding maxima in speed and efficiency of transport. The transport mechanism reported here has a remarkable resemblance to the flagellar propulsion of microorganisms which suggests its utility in biomimetic systems.

I. INTRODUCTION

Diffusion is a universal but slow mechanism for particle transport at finite temperatures. Solutions to the problem of enhancing the rate of transport beyond the diffusion limit are found at several scales in living systems. At the sub-cellular scale, special proteins called molecular motors transport macromolecules super-diffusively along microtubule tracks [1–3]. At the cellular scale, molecular motors induce collective motion of the intra-cellular fluid, a phenomenon known as cytoplasmic streaming [4–6]. At the extra-cellular scale collective motion of cilia, known as metachronal waves, transports visco-elastic fluids along channels and provides, alongside flagella, motility to whole organisms [7–9]. These *active* transport processes, by consuming internal sources of energy, are able to sustain gradients in entropy, and therefore, of particle concentration. Their ability to transport particles against concentration gradients and over free-energy barriers has numerous uses in biology [10–13].

It has been notoriously difficult to synthetically replicate the active transport solutions arrived at through many millions of years of natural selection. Instead, enhanced particle transport in physical and chemical contexts has largely been achieved by the input of external sources of energy through applied fields [14, 15]. With the coming together of physical, chemical and biological phenomena in the domain broadly termed as biomimetics there is a fresh interest in searching for transport mechanisms that are both active *and* synthetic. Their potential applications are numerous, including the removal of damaged cells [16] and the targeted delivery of drugs [17] and microscopic devices [18].

There are several challenges in designing active transport solutions at the microscale. First, energy has to be supplied locally to the transport engine. In contrast to the macroscale, extracting work out of a heat engine is unfeasible due to impossibility of maintaing heat baths at distinct temperatures [19]. The controlled release of chemical energy appears to be the most convenient method of energy supply and recent successful designs borrowed from biology in using adenosine triphosphate (ATP) as the source of energy [20, 21]. Second, the mechanical motion that results in transport has to be non-reciprocal, a result Purcell named as the "scallop theorem" [22]. This is a consequence of the dominance of viscous forces at the microscale, where forces, to an excellent approximation, are proportional to velocities, rather than to accelerations. Reciprocal motion of a single degree of freedom, then, produces zero net motion. Therefore, to produce net directed motion the mechanical forcing of the fluid has to be done using at least two degrees of freedom. Third, the magnitude of directed motion has to be sufficient to overcome diffusion. Fourth, in the absence of organizational structures like the cytoskeleton, mechanisms must be available in the transport engine itself to navigate in three dimensional space. Finally, for biomimetic applications the design has to be biocompatible, avoiding hazardous chemicals or strong external fields.

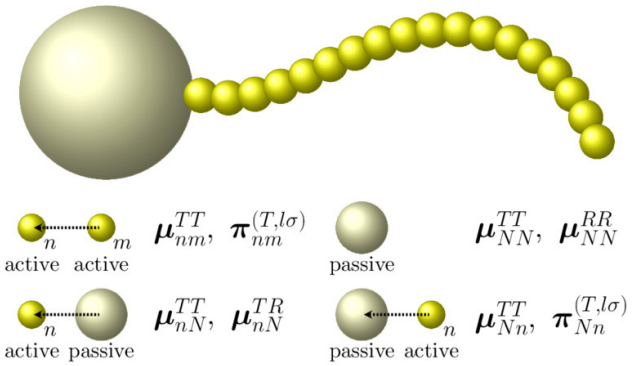

Figure 1. An active filament, consisting of $N-1$ active beads (small spheres), attached to a passive colloid (large sphere). The various hydrodynamic interactions between the N spheres, comprising the colloid-filament assembly, are shown alongside. See text for explanation of symbols.

Due to the paucity of local power injection mechanisms, enhanced transport at the micron scale is mainly achieved by applying external gradients of electrical [15], thermal [14] or concentration [23] fields. In one class of mechanisms, interactions between such externally applied fields and the particle boundary produces interfacial stresses that leads to particle transport, collectively referred to as phoretic motion [24]. Sen, Mallouk and co-workers realised that the phoretic mechanism could be utilised by internally generated field gradients, leading to their design of autophoretic colloidal particles that drew on the energy released by a catalytic reaction at the particle surface [25]. This has produced an explosion of research in autophoresis, and more generally, in utilising chemical energy in the solvent to transcend the diffusion limit. New autophoretic mechanisms include bubble propulsion [26] and redox reactions at the particle surface [27]. In another class of mechanisms, the externally applied fields act directly on the particles. Acoustic radiation pressure from ultrasonic standing waves has recently been used to transport micrometer size metallic rods [28]. Structural chirality has been exploited in nanopropellers that are driven by external magnetic fields [29]. Moving from rigid to flexible objects, the beating motion of a chain of paramagnetic beads driven by an oscillating magnetic field has been used to create propulsion engines reminiscent of cilia and flagella [30]. This, by no means, is a complete survey and the reader is referred to [31–34] for the state of the art.

Recently, a remarkable new class of material has been created in which internal sources of energy, provided by ATP in solution, is utilised to generate motion [21, 35]. The material is a mixture of microtubules, polymers that induce depletion interactions between them, and molecular motors. The microtubules self-assemble into filaments that beat spontaneously in the presence of ATP, driven by the motion of the molecular motors. Such active filaments have great potential for use in enhanced transport, as they utilize local sources of energy, are not bound by the scallop theorem, produce forces that are many times larger than their diffusive counterparts, and are biocompatible. Navigability is yet to be achieved using such active filaments.

Here we show that an active filament attached to a colloidal sphere provides an active transport solution that meets all the five desiderata listed above. We use a general model, that includes hydrodynamic interactions, to describe the active filament [36–38]. Sustained motion is produced by a balance of forces arising from the spontaneous activity, modeled as a distribution of stresslets along the filament length, and the elasticity of the filament. The exchange of momentum between fluid and filament and its local conservation in the fluid are taken into account through an integral representation of the fluid flow. Waveforms and beat periods obtained from this model [37] are in excellent agreement with experiment [21]. Our main results are that enhanced colloidal transport can be achieved through the active filament engine, that speed and efficiency of the transport depend on the dynamical steady states of the filament, that these steady states can be accurately classified using the filament writhe as an order parameter, and finally, that states yielding the greatest speed or efficiency can thus be identified. We discuss how navigation can be achieved by including a paramagnetic component in the colloid. We conclude by suggesting several biomimetic systems where our design can be put to use.

II. MODEL

Our model for the assembly of the active filament and the colloid consists of $n = 1, \ldots, N-1$ spherical active beads of radius b and center-of-mass coordinates $\mathbf{R}_n$ chained together by potentials and a single passive sphere of radius $b_c \gg b$ and center-of-mass coordinate $\mathbf{R}_N$. The filament is clamped to the surface of the colloid through constraint forces. A schematic is shown in Fig.(1). At low Reynolds number, Newton's equation of motion for the N spheres reduce to instantaneous balance of forces and torques,

$$\mathbf{F}_n + \mathbf{F}_n^b + \boldsymbol{\xi}_n^T = \mathbf{0}, \qquad \mathbf{T}_n + \mathbf{T}_n^b + \boldsymbol{\xi}_n^R = \mathbf{0}, \tag{1}$$

where $\mathbf{F}_n^b$ and $\mathbf{T}_n^b$ are the net body force and torque and $\boldsymbol{\xi}_n^T$ and $\boldsymbol{\xi}_n^R$ are the Brownian force and torque on the n-th sphere. $\mathbf{F}_n = \int \mathbf{f}\, dS_n$ and $\mathbf{T}_n = \int \boldsymbol{\rho}_n \times \mathbf{f}\, dS_n$ are the total hydrodynamic force and torque in terms of the integral of the traction $\mathbf{f} = \mathbf{n} \cdot \boldsymbol{\sigma}$, where $\boldsymbol{\rho}_n$ is the vector from the center of the n-th sphere to a point on its surface and $\boldsymbol{\sigma}$ is the Cauchy stress in the fluid.

The Cauchy stress is determined by solving the Stokes equation $\nabla \cdot \boldsymbol{\sigma} = 0$ for the fluid velocity $\mathbf{v}$ together with the incompressibility condition $\nabla \cdot \mathbf{v} = 0$ and the slip boundary conditions

$$\mathbf{v}(\mathbf{R}_n + \boldsymbol{\rho}_n) = \mathbf{V}_n + \boldsymbol{\Omega}_n \times \boldsymbol{\rho}_n + \mathbf{v}_n^{\mathcal{A}}(\boldsymbol{\rho}_n) \tag{2}$$

on the surface of the $N-1$ active spheres and the usual no-slip boundary condition on the surface of the colloid. The active slip $\mathbf{v}_n^{\mathcal{A}}(\boldsymbol{\rho}_n)$ is conveniently expanded in the complete orthogonal basis of irreducible tensorial spherical harmonics, $\mathbf{Y}^l(\hat{\boldsymbol{\rho}}) = (-1)^l \rho^{l+1} \boldsymbol{\nabla}^{(l)} \rho^{-1}$, as

$$\mathbf{v}_n^{\mathcal{A}}(\mathbf{R}_n + \boldsymbol{\rho}_n) = \sum_{l=1}^{\infty} A_l \mathbf{V}_n^{(l)} \cdot \mathbf{Y}^{(l-1)}(\hat{\boldsymbol{\rho}_n}) \tag{3}$$

where $A_l = 1/(l-1)!(2l-3)!!$ is a normalization. The expansion coefficients $\mathbf{V}_n^l$ are tensors of rank l, irreducible in their last $l-1$ indices, and can thus be expressed as the sum of three irreducible tensors $\mathbf{V}_n^{(ls)}$, $\mathbf{V}_n^{(la)}$ and $\mathbf{V}_n^{(lt)}$, of rank l, $l-1$ and $l-2$ respectively. They represent the symmetric traceless, antisymmetric and

pure trace parts of $\mathbf{V}_n^{(l)}$, $\mathbf{V}^{(ls)} = \overline{\mathbf{V}_n^{(l)}}$, $\mathbf{V}^{(la)} = \overline{\boldsymbol{\epsilon}\cdot\mathbf{V}_n^{(l)}}$ and $\mathbf{V}_n^{(lt)} = \overline{\boldsymbol{\delta}:\mathbf{V}_n^{(l)}}$. We use the notation $\mathbf{V}_n^{(l\sigma)}$, with $\sigma = s, a, t$ to denote these irreducible parts, each of which are of the dimension of velocity. It is assumed that the form of the slip and, therefore, the values of the coefficients are specified. The velocity, $\mathbf{V}_n$, and angular velocity, $\boldsymbol{\Omega}_n$, are to be determined, given the slip coefficients and the external and Brownian forces and torques.

From linearity of Stokes flow and the boundary conditions, it follows that the hydrodynamic forces and torques must be of the form

$$\begin{aligned}\mathbf{F}_n &= -\boldsymbol{\gamma}_{nm}^{TT}\cdot\mathbf{V}_m - \boldsymbol{\gamma}_{nm}^{TR}\cdot\boldsymbol{\Omega}_m - \boldsymbol{\gamma}_{nm}^{(T,l\sigma)}\cdot\mathbf{V}_m^{(l\sigma)},\\ \mathbf{T}_n &= -\boldsymbol{\gamma}_{nm}^{RT}\cdot\mathbf{V}_m - \boldsymbol{\gamma}_{nm}^{RR}\cdot\boldsymbol{\Omega}_m - \boldsymbol{\gamma}_{nm}^{(R,l\sigma)}\cdot\mathbf{V}_m^{(l\sigma)},\end{aligned}$$

where the summation convention is implied for all repeated indices and the slip coefficients $\mathbf{V}_N^{(l\sigma)}$ of the colloid are all identically zero. The $\boldsymbol{\gamma}_{nm,}^{\alpha\beta}$, with $\alpha, \beta = T, R$, are the usual Stokes friction tensors, yielding drag forces proportional to $\mathbf{V}_m$ and $\boldsymbol{\Omega}_m$. The terms proportional to $\mathbf{V}_m^{l\sigma}$ are active contributions to the forces and torques due to the slip $\mathbf{v}_m^{\mathcal{A}}$. The $\boldsymbol{\gamma}_{nm}^{(T,l\sigma)}$ and $\boldsymbol{\gamma}_{nm}^{(R,l\sigma)}$ are slip friction tensors associated with the $l\sigma$ mode of the slip velocity. A method for calculating these slip friction tensors in terms of Green's functions of Stokes flow has been provided recently [39, 40] and the reader is referred there for further details.

Combining the above with Newton's equations, ignoring the Brownian contributions and solving the resulting balances yields the following *explicit* equations for the velocity and angular velocity

$$\begin{aligned}\mathbf{V}_n &= \boldsymbol{\mu}_{nm}^{TT}\cdot\mathbf{F}_m^b + \boldsymbol{\mu}_{nm}^{TR}\cdot\mathbf{T}_m^b + \sum_{l\sigma=1s}^{\infty}\boldsymbol{\pi}_{nm}^{(T,l\sigma)}\cdot\mathbf{V}_m^{(l\sigma)}\\ \boldsymbol{\Omega}_n &= \boldsymbol{\mu}_{nm}^{RT}\cdot\mathbf{F}_m^b + \boldsymbol{\mu}_{nm}^{RR}\cdot\mathbf{T}_m^b + \sum_{l\sigma=1s}^{\infty}\boldsymbol{\pi}_{nm}^{(R,l\sigma)}\cdot\mathbf{V}_m^{(l\sigma)}.\end{aligned}$$

Here, $\mathbf{V}_n^{\mathcal{A}} = \mathbf{V}_n^{(1s)}$ is the active translational velocity, $\boldsymbol{\Omega}_n^{\mathcal{A}} = b^{-1}\mathbf{V}_n^{2a}$ is the active angular velocity, $\boldsymbol{\mu}_{nm}^{\alpha\beta}$ are the usual mobility tensors and $\boldsymbol{\pi}_{nm}^{(\alpha,l\sigma)}$ are the propulsion tensors introduced in [41]. The relation between the mobility, slip friction and propulsion tensors is easily verified to be

$$\begin{aligned}-\boldsymbol{\pi}_{nm}^{(T,l\sigma)} &= \boldsymbol{\mu}_{nq}^{TT}\cdot\boldsymbol{\gamma}_{qm}^{(T,l\sigma)} + \boldsymbol{\mu}_{nq}^{TR}\cdot\boldsymbol{\gamma}_{qm}^{(R,l\sigma)}\\ -\boldsymbol{\pi}_{nm}^{(R,l\sigma)} &= \boldsymbol{\mu}_{nq}^{RT}\cdot\boldsymbol{\gamma}_{qm}^{(T,l\sigma)} + \boldsymbol{\mu}_{nq}^{RR}\cdot\boldsymbol{\gamma}_{qm}^{(R,l\sigma)}\end{aligned}$$

We evaluate all the above tensors in the pair-approximation, as is commonly done in bead-spring models of polymers. The translational mobility has the familiar Rotne-Prager form. Explicit forms of the remaining tensors are provided in the Appendix.

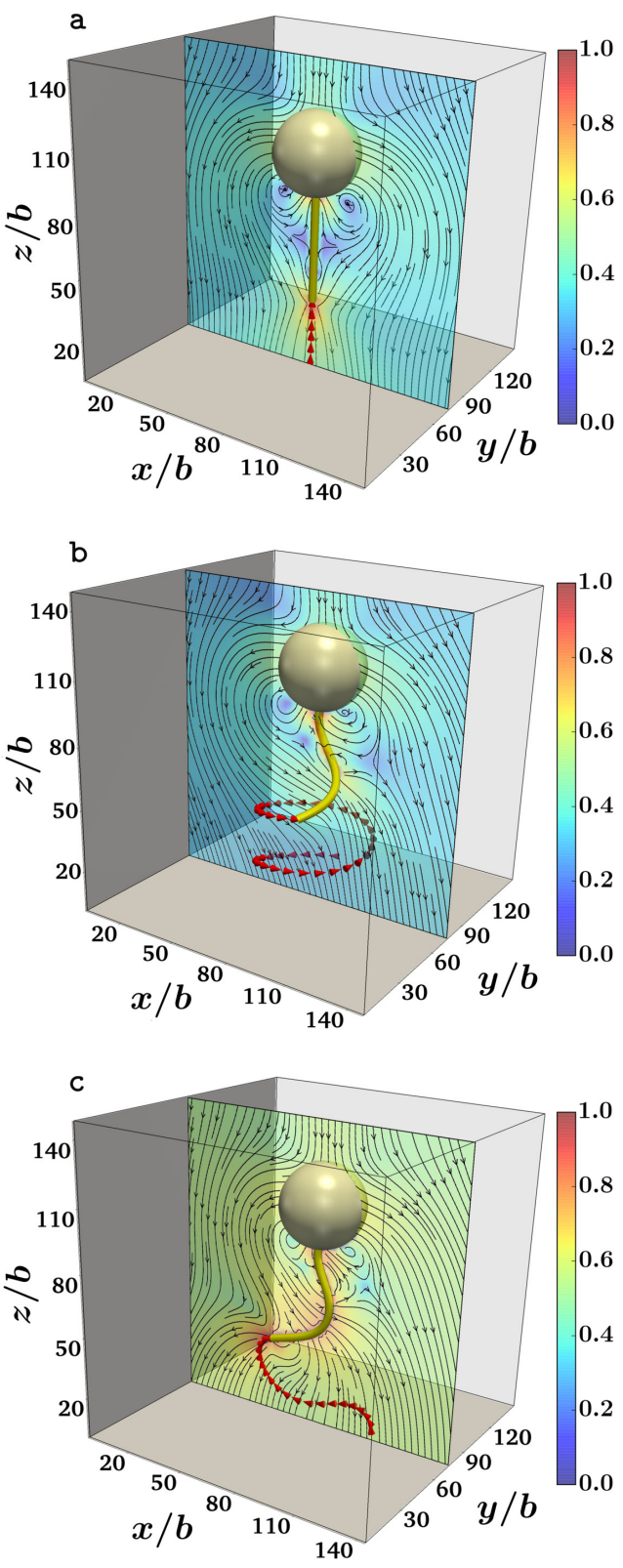

Figure 2. Dynamical states of the filament-colloid assembly with varying activity $\mathcal{A}$ showing the the *linear* state at $\mathcal{A}$=10 in panel (a), the *helical* state with $\mathcal{A}$=40 in panel (b) and the *planar* state at $\mathcal{A}$=80 in panel (c). Fluid streamlines are shown in a plane passing through the equator of the colloid, coloured by the logarithm of the magnitude of fluid velocity normalised by its maximum. The red cones show the trajectory of the filament terminus.

The above represents the equations of motion that allow for the most general forms of surface activity. Here, we restrict ourselves to the simplest *apolar, achiral* model for slip flow, in which the only non-zero tensorial harmonic mode corresponds to $l\sigma = 2s$, which we parametrize as

$$\mathbf{V}_m^{(2s)} = V_0^{(2s)}(\hat{\mathbf{t}}_m\hat{\mathbf{t}}_m - \frac{1}{3}\boldsymbol{\delta}) \tag{4}$$

We chose the principal value $V_0^{(2s)}$ of this second-rank tensor to be positive and its principal axis to be along the local tangent $\hat{\mathbf{t}}_m$ to the filament. The rich dynamical behaviour of this minimally active filament has qualitative and quantitative similarities with active filament systems realized experimentally [37].

The body force $\mathbf{F}_n^b$ between the, now minimally active, beads is obtained from the gradient of the potential $U = U^C + U^E + U^S$ which, in sequence, are potentials enforcing connectivity, semi-flexibility and self-avoidance. The connectivity potential is the two body harmonic spring potential $U^C(\mathbf{R}_m, \mathbf{R}_{m+1}) = \frac{1}{2}k(r-b_0)^2$, where b_0 is the equilibrium bond and $r = |\mathbf{R}_m - \mathbf{R}_{m+1}|$. The three-body elastic potential $U^E = \bar{\kappa}(1-\cos\phi)$ penalizes departures of the angle ϕ between consecutive bond vectors from its equilibrium value of zero. The rigidity parameter $\bar{\kappa}$ is related to the bending rigidity as $\kappa = b_0\bar{\kappa}$. Steric effects are included through the Weeks-Chandler-Anderson potential which vanishes if the distance between beads $r_{mn} = |\mathbf{R}_m - \mathbf{R}_n|$ exceeds $r_{\min}$. We assume constraint torques that result in the vanishing rotation of the beads. Their values are obtained from the torque balance equation with bead angular velocities set to zero. The body force $\mathbf{F}_N^b$ and torque $\mathbf{T}_N^b$ on the colloid arise from the constraint forces that clamp the filament to its surface. These are discussed more fully in the Appendix.

With these specifications, the equation of motion of the active filament is

$$\dot{\mathbf{R}}_n = \underbrace{\boldsymbol{\mu}_{nN}^{TT}\cdot\mathbf{F}_N^b + \boldsymbol{\mu}_{nN}^{TR}\cdot\mathbf{T}_N^b}_{\text{colloid}} + \underbrace{\boldsymbol{\mu}_{nm}^{TT}\cdot\mathbf{F}_m^b}_{\text{elasticity}} + \underbrace{\boldsymbol{\pi}_{nm}^{(T,2s)}\cdot\mathbf{V}_m^{(2s)}}_{\text{activity}} \tag{5}$$

In the absence of the colloid and as the activity goes to zero, the filament equation of motion approaches the Zimm model, where $L = (N-2)b_0$ is the length of the filament [36]. The rigid body motion of the active colloid is obtained from the pair of equations

$$\mathbf{V}_N = \boldsymbol{\mu}_{NN}^{TT}\cdot\mathbf{F}_N^b + \boldsymbol{\mu}_{Nn}^{TT}\cdot\mathbf{F}_n^b + \boldsymbol{\pi}_{Nn}^{(T,2s)}\cdot\mathbf{V}_n^{(2s)} \tag{6a}$$

$$\boldsymbol{\Omega}_N = \underbrace{\boldsymbol{\mu}_{NN}^{RR}\cdot\mathbf{T}_N^b}_{\text{colloid}} + \underbrace{\boldsymbol{\mu}_{Nn}^{RT}\cdot\mathbf{F}_n^b}_{\text{elasticity}} + \underbrace{\boldsymbol{\pi}_{Nn}^{(R,2s)}\cdot\mathbf{V}_n^{(2s)}}_{\text{activity}} \tag{6b}$$

The relative importance of activity is quantified by its ratio with elasticity,

$$\mathcal{A} = \frac{|\boldsymbol{\gamma}_{nn}^{(T,2s)}\cdot\mathbf{V}_n^{(2s)}|}{|\mathbf{F}_n^b|} \approx \frac{\eta b^2 L V_0^{(2s)}}{\kappa} \tag{7}$$

Activity introduces a new relaxation rate $\Gamma_s = V_0^{2S}/\eta L^3$ in addition to rate of elastic relaxation $\Gamma_\kappa = \kappa/\eta L^4$. The position and orientation of the colloid changes according to the kinematic equations $\dot{\mathbf{R}}_N = \mathbf{V}_N, \quad \dot{\mathbf{p}}_N = \boldsymbol{\Omega}_N \times \mathbf{p}_N$. These overdamped equations take into account the forces and torques mediated by flow generated by the motion *and* activity of the beads and the motion of the colloid. We integrate the above set of equations numerically to obtain the dynamics of the colloid-filament assembly.

III. RESULTS

We now present the results of our numerical study of the dynamics of the colloid-filament assembly, as the "activity number" $\mathcal{A}$, the relative size of the colloid b_c/b and the length L of the filament are varied.

Fig. (2) shows three typical states of motion of the assembly, with activity number increasing from top to

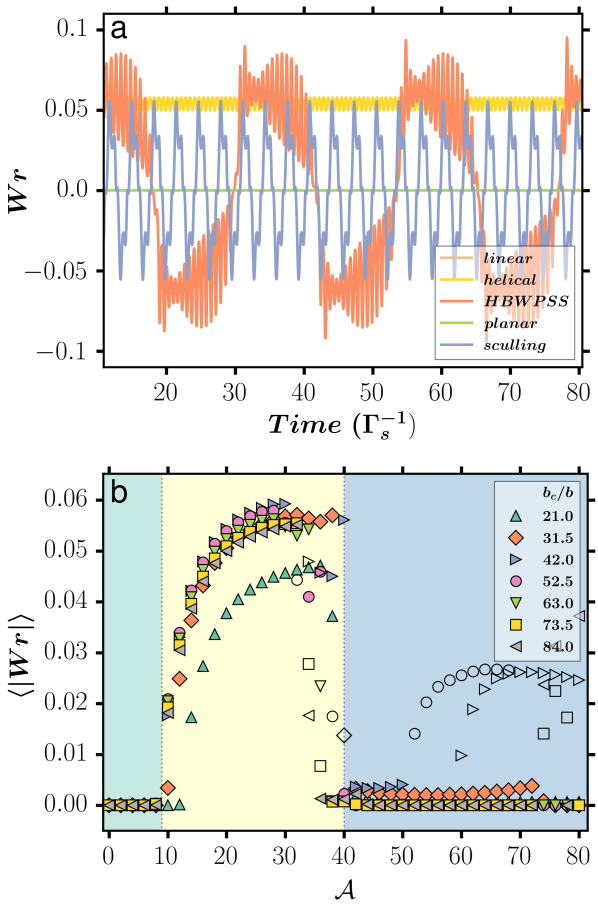

Figure 3. The time series of writhe, panel (a), and mean of its absolute value as a function of activity $\mathcal{A}$ for $L = 70b$ in panel (b). The background colors are to mark the region of linear (green), helical (yellow) and planar (blue) state. The empty symbols in helical and planar region are for HBWPSS and sculling state respectively.

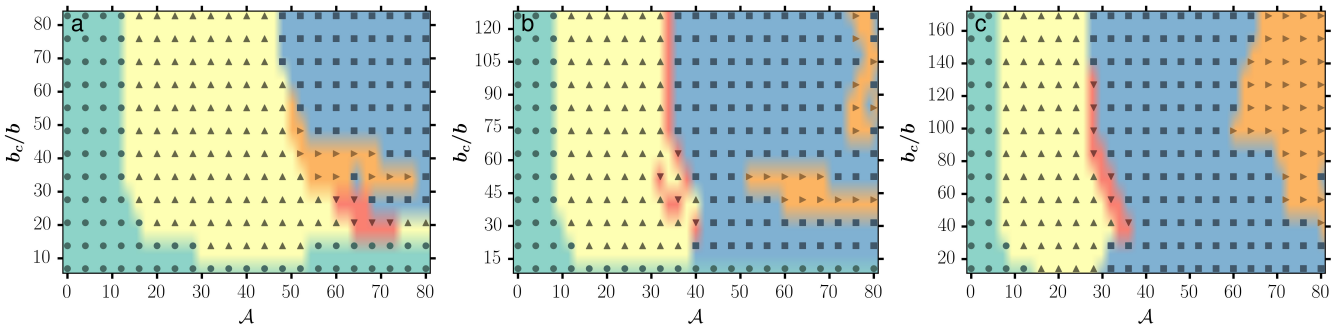

Figure 4. Phase diagram of the non-equilibrium stationary states of the filament as a function of relative size of colloid b_c/b and dimension less quantity $\mathcal{A}$ for three different filament lengths $L = 46b$ (a), $L = 70b$ (b), $L = 94b$ (c). Symbols represent the following: linear state (circle), helical state (triangle up), helical beating with periodic switching of sign (triangle down), planar (square) and sculling like beating (triangle right). The colours are guides to the eye.

bottom, together with a planar section of the fluid flow around the assembly. Panel (a) shows the simplest dynamical state, where transport of the colloid occurs without any deformation of the filament. Panel (b) shows a state where the filament moves rigidly in an aplanar corkscrew-like motion, its tip tracing out a helix as it transports the colloid. The trace of the tip is shown by the red cones. Panel (c) shows a state in which the filament moves flexibly in a plane, its tip tracing out an "s" shape while it transports the colloid (see Movie 1 of the Supplemental Material [42]). These sequence of distinct states of motion of the filament is what is observed when the filament is clamped at a point in an otherwise unbounded fluid [37]. The principal difference is in the values of the activity number $\mathcal{A}$ at which the transitions take place, a difference we attribute to the modified hydrodynamic interactions between parts of the filament arising from the reflection of the flow field by the surface of the colloid.

These sequence of states arise from the balance of the three kinds of forces (and torques) acting on each bead of our filament: the conservative force from the potentials and the two dissipative forces, one from the drag and another from the activity. The nature of the active force, for positive $V_0^{(2s)}$, is such that it produces motion *opposite* to the direction of the signed curvature. Therefore, as activity is increased, states with increasing amounts of curvature appear in sequence. Thus, in Fig. (2), we first see a linear propulsive state, then a state in which the curvature is a fixed function of time, and finally, states in which the curvature is a period function of time.

A quantitative demarcation of these distinct non-equilibrium steady states requires the introduction of an order parameter. We use the filament writhe [43]

$$Wr = \frac{1}{4\pi}\int_C\int_C d\mathbf{r}_1 \times d\mathbf{r}_2 \cdot \frac{\mathbf{r}_1 - \mathbf{r}_2}{|\mathbf{r}_1 - \mathbf{r}_2|^3} \qquad (8)$$

as an order parameter which can effectively distinguish these non-equilibrium steady states. The integrations over points $\mathbf{r}_1$ and $\mathbf{r}_2$ on the filament contour are replaced by summations over the number of beads. In Fig. (3), top panel, we show the time series of writhe for the states shown in Fig. (2) together with two additional states that are identified through the order parameter. In the linear and planar states, the writhe is identically zero. The helical state has a non-zero mean value of writhe, with superimposed small amplitude oscillations. The two remaining states have periodic oscillations in which the writhe averages to zero over the cycle, but otherwise oscillates in sign. In the first of these states, the filament rotates as in the helical state but in opposite directions during each half of the cycle, which consists of several periods of *helical* motion. For lack of a better description, we call this state helical beating with periodic switching of sign (HBWPSS). The second of these states shows a motion reminiscent of sculling, in which the filament beats in a plane that changes orientation over the cycle (see Movie 2 of the Supplemental Material [42]). In Fig. (3), bottom panel, we show the variation of mean of the absolute value of writhe as a function of activity number, for different ratios of the colloid radius and filament length. This clarifies the sequence in which the states appear. The linear states are stable at small values of activity, being then replaced by the helical, HBWPSS and sculling states of non-zero mean writhe as the activity is increased. At yet larger values of activity, these states are unstable and the planar state is generally favoured. The non-equilibrium state diagram, thus obtained, is shown in Fig. (4) for three different lengths of the filament. The majority of the state diagram is occupied by the three states shown in Fig. (2) and careful parameters choices are required to locate the HBWPSS and sculling states.

How does the speed and efficiency of colloidal transport vary across these states? To answer this quantitatively we define, first, a measure of efficiency, which is the ratio of the power expended in transporting a passive colloid with velocity $\mathbf{V}$ to that expended in the filament-colloid assembly at the same velocity,

$$\epsilon = \frac{\mathbf{V}_N \cdot \boldsymbol{\gamma}^{TT}_{NN} \cdot \mathbf{V}_N}{\dot{W}} \tag{9}$$

Definitions of this kind were first used by Lighthill [44] in his study of the squirming motion of a sphere. In Fig. (5) we show the variation of the speed (top panel) and efficiency (bottom pane) of transport as a function of activity number for varying size of the colloid. Transport speed is enhanced, more or less monotonically, by decreasing the size of the colloid, but transport speed varies non-monotonically with activity. States with zero mean writhe yield greater speeds than those without, as the chemo-mechanical work done is partially stored in the form of elastic energy in the latter class of states, making less of it available for transport. This picture is borne out in the variation of the efficiency ϵ, where shorter filaments in states with smaller conformational deformations have greater efficiencies of transport. This understanding of speed and efficiency is necessary for optimizing the design parameters of such assemblies in possible biomimetic applications.

The non-equilibrium stationary states are fixed points or limit cycles of the overdamped equations of motion, Eq. (5) and Eq. (6a). It is straightforward to analyze the linear stability of the filament as a function of activity. It is by now well-understood that the apolar active filaments are linearly unstable above a certain threshold value of activity [36–38]. This linear instability arises from the convective effect of the dipolar flow produced by the filament. Here, we revisit the stability analysis of [37], taking into account the presence of the colloid and the no-slip boundary conditions imposed on it. We numerically compute the Jacobian in the linear state of the filament and from it, obtain its largest eigenvalues, discarding the six eigenvalues that correspond to rigid body motion. The result of this analysis is shown in Fig. (6). In the top panel, we show the evolution of the eigenvalues as a function of activity for filament length $L = 70b$ as we move from left to right of the middle panel in Fig. (4) at $b_c = 42b$. We see the familiar coalescence of eigenvalues to produce a complex conjugate pair, which then acquires a positive real part with increasing activity. This is similar to the Hopf bifurcation seen in the case of filaments clamped to a point in three dimensions [37]. The bottom panel in Fig. (6) shows the eigenvalues as we move from the bottom to top of the phase diagram shown in the middle panel of Fig. (4) at $\mathcal{A} = 20$. Here the eigenvalues remain real but change sign from negative to positive. This corresponds to a standard instability, rather than a Hopf bifurcation.

The presence of the colloid alters the value of the activity numbers at which the bifurcations occur, but leaves unaltered their sequence. This is because the flow reflected by the colloid contributes only a correction to the hydrodynamic interaction mediated by the flow produced by the beads, as an inspection of the explicit form of this correction, provided in the Appendix, will confirm.

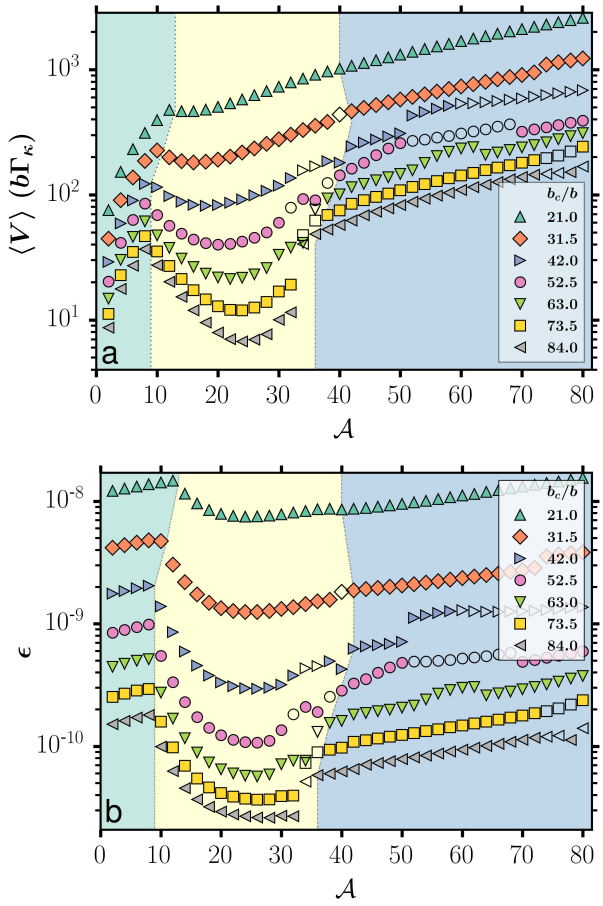

Figure 5. The average translational speed a) and Efficiency of transport b) of the colloid as a function of $\mathcal{A}$ for different colloid radius, b_c for filament length $L = 70b$. The background colors are to mark the region of linear (green), helical (yellow) and planar (blue) state. The empty symbols in helical and planar region are for HBWPSS and sculling state respectively.

IV. DISCUSSIONS

In earlier theoretical and simulation investigations on the cargo transport by active filament, the effect of activity was introduced by applying a local force on each bead, thus ignoring all hydrodynamic interactions [45]. On the other hand, the work presented here describes motion induced by non-local hydrodynamic flow, resulting from active forcing, that explicitly take into account force balance and torque balance in a three dimensional model of colloid-filament assembly.

We show that active filament consisting of chemo-mechanically active apolar beads can transport a colloid to which it is clamped, in a viscous fluid. With the over damped hydrodynamic equation of motions, we investigate the influence of the length of the filament, the strength of activity and the colloid radius on its motion. We identify five different conformational states of the filament, as opposed to three in the case of a fila-

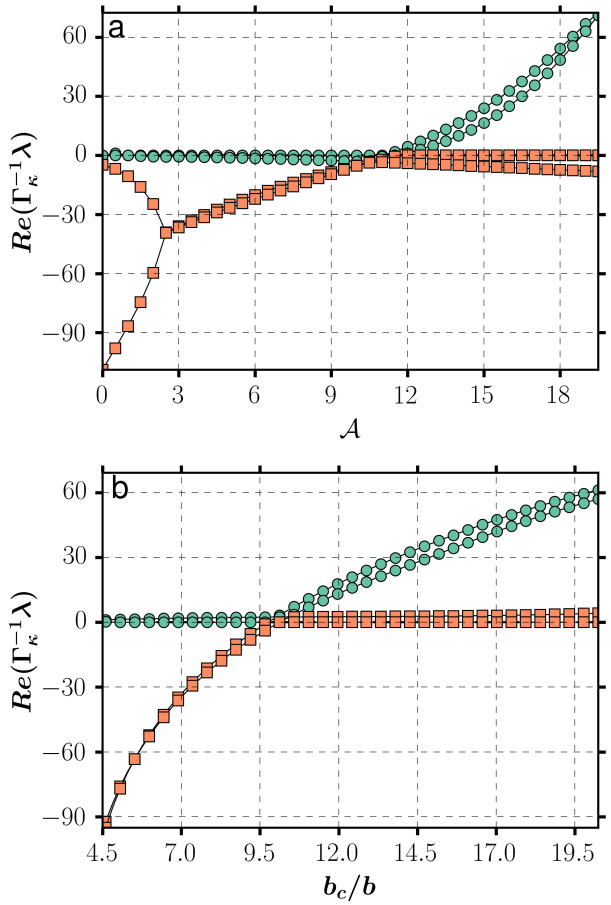

Figure 6. Linear stability analysis: The largest eigenvalues of stability matrix as function of activity number, $\mathcal{A}$ for $b_c = 42b$ (a), and relative colloid radius b_c/b for $\mathcal{A} = 20$ (b). Here the length of the filament is $L = 70b$.

ment clamped to a stationary point [37]. It is shown that the transport speed and efficiency depend on these dynamical states of the filament. For a given stiffness of the filament, the speed of transport is maximum for the planar beating conformation whereas the efficiency of transport is greatest in the case of linear conformation. The efficiency of the transport of the colloid is found to be in the order of 10^{-9}, similar to that observed in the transport of Au-Pt nano-rods in H_20_2 solution [33, 46]. The power to be delivered locally ($\sim 10^{-15}$ W) and the speed that can be achieved (several $\mu m/s$) are reasonable and are more important parameters for application. For a given stiffness and activity strength V_0^{2s} the efficiency and speed are higher for lower filament lengths (data not shown). However, directional stability increases with the filament length since rotational diffusivity of an object decreases as the cube of its size. Thus we expect all regimes of the colloid filament system to be of relevance applications. The propulsion efficiency is significantly lower than in bacteria, where it varies in the range $\sim 10^{-2} - 10^{-4}$. This is due to the very high efficiency of ATPase as an engine, almost 50% of whose energy is available for work. Thus, though propulsion is a small component of the overall energy budget of an organism (Purcell has memorably likened it to "driving a Datsun in Saudi Arabia" [22]), we believe that there is room to improve the efficiency of current active transport mechanisms.

Though we have limited our discussion here to a system consisting of one colloid and one filament, the equations of motion presented here are general and can analyse more complex configurations of filaments in an individual swimmer and a collection of swimmers. Immediate extensions could be two filament systems like the flagella geometry of algae Chlamydomonas, multiple filaments working synchronously in a viscous fluid and collection of such swimmers. Though the collective dynamics of a suspension of spheres which produce constant dipolar flows are by now well-understood, here, the far field produced by the colloid-filament assembly is time-dependent. The collective dynamics of such "oscillatory dipoles" will show new features, such as hydrodynamic synchronization, that are absent in their time-independent counterparts [47, 48]. It should be noted that the effects of wall can significantly change the dynamics of the swimmer in the micron scale [49] and the states of the swimmer obtained here could be altered by such boundary conditions. We will present a systematic study of these aspects in future.

Our focus in this work has been to propose a mechanism for transport using an active filament. Mechanisms for navigation are crucial for applications in areas such as biomedicine. One possible navigation mechanism is through a paramagnetic component in the colloid which can then be controlled by an external magnetic field [50]. This and other mechanisms for navigation will be presented in a future study.

SUPPLEMENTARY MATERIAL

Movie-1[42]: This movie displays the temporal behavior of the dynamical states of the colloid-filament assembly with fluid streamlines.

Movie-2[42]: This movie displays the dynamics of colloid-filament assembly with filament writhe.

ACKNOWLEDGMENTS

We thank S. Ghose, Sachin Krishnan, A. Laskar, Rajeev Singh and Rajesh Singh for helpful discussions. RA wishes to thank the Department of Atomic Energy, Government of India for supporting his research. Numerical simulations were performed on the Annapurna and HPCE clusters at The Institute of Mathematical Sciences and IIT Madras, respectively.

APPENDIX

Mobility and propulsion tensors

The mobility tensors, are defined as

$$8\pi\eta\boldsymbol{\mu}_{nm}^{TT}(\mathbf{R}_n,\mathbf{R}_m)=\begin{cases}\mathcal{F}_n^0\mathcal{F}_m^0\mathbf{G}(\mathbf{R}_n,\mathbf{R}_m) & n\neq m\\ \frac{4}{3}b_n^{-1}\boldsymbol{\delta} & n=m\end{cases}$$

$$8\pi\eta\boldsymbol{\mu}_{nm}^{TR}(\mathbf{R}_n,\mathbf{R}_m)=\begin{cases}\frac{1}{2}\boldsymbol{\nabla}_m\times\mathbf{G}(\mathbf{R}_n,\mathbf{R}_m) & n\neq m\\ \mathbf{0} & n=m\end{cases}$$

$$8\pi\eta\boldsymbol{\mu}_{nm}^{RT}(\mathbf{R}_n,\mathbf{R}_m)=\begin{cases}\frac{1}{2}\boldsymbol{\nabla}_n\times\mathbf{G}(\mathbf{R}_n,\mathbf{R}_m) & n\neq m\\ \mathbf{0} & n=m\end{cases}$$

$$8\pi\eta\boldsymbol{\mu}_{nm}^{RR}(\mathbf{R}_n,\mathbf{R}_m)=\begin{cases}\frac{1}{4}\boldsymbol{\nabla}_n\times\boldsymbol{\nabla}_m\times\mathbf{G}(\mathbf{R}_n,\mathbf{R}_m) & n\neq m\\ b_n^{-3}\boldsymbol{\delta} & n=m\end{cases}$$

,

where $\mathbf{G}$ is the Green's function for Stokes flow in un unbounded medium,

$$G_{ij}(\mathbf{R}_n,\mathbf{R}_m)=\frac{\delta_{ij}}{r}+\frac{r_i r_j}{r^3},$$

with $\mathbf{r}=\mathbf{R}_n-\mathbf{R}_m$. The propulsion tensors which relate $\mathbf{V}_m^{(l\sigma)}$, the coefficient of the traction fields on the boundary of the m-th particle to the rigid body motion are defined as

$$8\pi\eta\boldsymbol{\pi}_{nm}^{(T,2s)}=\begin{cases}c\mathcal{F}_n^0\mathcal{F}_m^1\boldsymbol{\nabla}_m\mathbf{G}(\mathbf{R}_n,\mathbf{R}_m) & n\neq m\\ \mathbf{0} & n=m\end{cases}$$

$$8\pi\eta\boldsymbol{\pi}_{nm}^{(R,2s)}=\begin{cases}\frac{c}{2}\nabla_n\times\boldsymbol{\nabla}_m\mathbf{G}(\mathbf{R}_n,\mathbf{R}_m) & n\neq m\\ \mathbf{0} & n=m\end{cases}$$

and $\mathcal{F}_n^l=(1+\frac{b_n^2}{4l+6}\boldsymbol{\nabla}_n^2)$ is the operator.

The finite size correction to the mobility and propulsion tensors due to the colloid are

$$8\pi\eta\boldsymbol{\mu}_{nm}^{TT}(\mathbf{R}_n,\mathbf{R}_m)=\mathcal{F}_n^0\mathcal{F}_m^0\mathbf{G}(\mathbf{R}_n,\mathbf{R}_m)$$
$$+\mathcal{F}_n^0\mathcal{F}_N^1\boldsymbol{\nabla}_N\mathbf{G}(\mathbf{R}_n,\mathbf{R}_N)\cdot(-c_0\mathcal{F}_N^1\mathcal{F}_m^0\boldsymbol{\nabla}_N\,\mathbf{G}(\mathbf{R}_N,\mathbf{R}_m))$$

$$8\pi\eta\boldsymbol{\pi}_{nm}^{(T,2s)}(\mathbf{R}_n,\mathbf{R}_m)=c\mathcal{F}_n^0\mathcal{F}_m^1\boldsymbol{\nabla}_m\mathbf{G}(\mathbf{R}_n,\mathbf{R}_m)$$
$$+\mathcal{F}_n^0\mathcal{F}_N^1\boldsymbol{\nabla}_N\mathbf{G}(\mathbf{R}_n,\mathbf{R}_N)\cdot(-c_0\mathcal{F}_N^1\mathcal{F}_m^1\,\boldsymbol{\nabla}_N\boldsymbol{\nabla}_m\mathbf{G}(\mathbf{R}_N,\mathbf{R}_m))$$

Constraint forces

The filament is clamped to the surface of the colloid particle. The clamping boundary conditions are implemented by fixing the last bead of the filament to the surface of the colloid and allowing the second last bead to move only along the radial direction,

$$\dot{\mathbf{R}}_{N-1}=\mathbf{V}_N+\boldsymbol{\Omega}_N\times(\mathbf{R}_{N-1}-\mathbf{R}_N)$$
$$(1-\hat{\mathbf{d}}\hat{\mathbf{d}})\cdot\Big(\mathbf{V}+\boldsymbol{\Omega}\times\mathbf{d}\Big)=(1-\hat{\mathbf{d}}\hat{\mathbf{d}})\cdot\dot{\mathbf{R}}_{N-2}$$

here $\mathbf{d}=\mathbf{R}_{N-2}-\mathbf{R}_N$ and $\hat{\mathbf{d}}=\mathbf{d}/|\mathbf{d}|$. To enforce the clamped boundary conditions on colloid, two constraint forces $\mathbf{F}_{N-1}^c$ and $\mathbf{F}_{N-2}^c$ are applied on the last and second last bead of the filament. These two constraint forces are obtained by solving the above constraint equations self-consistently. The force on the colloid particle is the negative sum of these constraint forces. Therefore the force and torque on the colloid particle are

$$\mathbf{F}_N=-(\mathbf{F}_{N-1}^c+\mathbf{F}_{N-2}^c)$$
$$\mathbf{T}_N=(\mathbf{R}_{N-1}-\mathbf{R}_N)\times\mathbf{F}_{N-1}^c+(\mathbf{R}_{N-2}-\mathbf{R}_N)\times\mathbf{F}_{N-2}^c$$

Power dissipation

The power dissipated into the fluid by the colloid-filament assembly is

$$\begin{aligned}\dot{W}&=\sum_n-\int\mathbf{f}_n(\mathbf{R}_n+\boldsymbol{\rho}_n)\cdot\mathbf{v}(\mathbf{R}_n+\boldsymbol{\rho}_n)\,dS_n\\&=\sum_n(-\mathbf{V}_n\cdot\mathbf{F}_n^{(1s)}-\boldsymbol{\Omega}_n\cdot\mathbf{F}_n^{(2a)}+\mathbf{V}_n^{(l\sigma)}\cdot\mathbf{F}_n^{(l\sigma)})\\&=\sum_n(\mathbf{V}_n\cdot\mathbf{F}_n^b+\boldsymbol{\Omega}_n\cdot\mathbf{T}_n^b)+\sum_{n,m}\mathbf{V}_n^{(l\sigma)}\cdot\boldsymbol{\gamma}_{nm}^{(l\sigma,l'\sigma')}\cdot\mathbf{V}_m^{(l'\sigma')}\end{aligned}$$

The equations of motion of the filament beads and colloid particle are integrated by numerically. We use spring constant $k=5.0$, equilibrium bond length $b_0=2b$, rigidity parameter $\bar{\kappa}=1.6$. We chose the number of beads N in the range 24 to 48 and $V_0^{(2s)}$ in the range 0 to 2.72.

[1] TJ Mitchison and LP Cramer, "Actin-based cell motility and cell locomotion," Cell **84**, 371–379 (1996).

[2] Ronald D Vale, "The molecular motor toolbox for intracellular transport," Cell **112**, 467–480 (2003).

[3] Shenshen Wang and Peter G Wolynes, "Active contractility in actomyosin networks," Proceedings of the National Academy of Sciences **109**, 6446–6451 (2012).

[4] Herwigo Gutzeit and Roswitha Koppa, "Time-lapse film analysis of cytoplasmic streaming during late oogenesis of drosophila," Development **67**, 101–111 (1982).

[5] William E Theurkauf *et al.*, "Premature microtubule-dependent cytoplasmic streaming in cappuccino and spire mutant oocytes," Science **265**, 2093–2093 (1994).

[6] Philipp Khuc Trong, Jochen Guck, and Raymond E Goldstein, "Coupling of active motion and advection shapes intracellular cargo transport," Physical review letters **109**, 028104 (2012).

[7] Martin B Short, Cristian A Solari, Sujoy Ganguly, Thomas R Powers, John O Kessler, and Raymond E Goldstein, "Flows driven by flagella of multicellular organisms enhance long-range molecular transport," Proceedings of the National Academy of Sciences **103**, 8315–8319 (2006).

[8] Douglas R Brumley, Marco Polin, Timothy J Pedley, and Raymond E Goldstein, "Hydrodynamic synchronization and metachronal waves on the surface of the colonial alga volvox carteri," Physical review letters **109**, 268102 (2012).

[9] Jens Elgeti and Gerhard Gompper, "Emergence of metachronal waves in cilia arrays," Proceedings of the National Academy of Sciences **110**, 4470–4475 (2013).

[10] Laura R Serbus, Byeong-Jik Cha, William E Theurkauf, and William M Saxton, "Dynein and the actin cytoskeleton control kinesin-driven cytoplasmic streaming in drosophila oocytes," Development **132**, 3743–3752 (2005).

[11] Kazunobu Sawamoto, Hynek Wichterle, Oscar Gonzalez-Perez, Jeremy A Cholfin, Masayuki Yamada, Nathalie Spassky, Noel S Murcia, Jose Manuel Garcia-Verdugo, Oscar Marin, John LR Rubenstein, *et al.*, "New neurons follow the flow of cerebrospinal fluid in the adult brain," Science **311**, 629–632 (2006).

[12] EA Gaffney, H Gadêlha, DJ Smith, JR Blake, and JC Kirkman-Brown, "Mammalian sperm motility: observation and theory," Annual Review of Fluid Mechanics **43**, 501–528 (2011).

[13] Laurence G Wilson, Lucy M Carter, and Sarah E Reece, "High-speed holographic microscopy of malaria parasites reveals ambidextrous flagellar waveforms," Proceedings of the National Academy of Sciences **110**, 18769–18774 (2013).

[14] Stefan Duhr and Dieter Braun, "Why molecules move along a temperature gradient," Proceedings of the National Academy of Sciences **103**, 19678–19682 (2006).

[15] William Bailey Russel, Dudley Albert Saville, and William Raymond Schowalter, *Colloidal dispersions* (Cambridge university press, 1992).

[16] Richard P Feynman, "There's plenty of room at the bottom," Engineering and science **23**, 22–36 (1960).

[17] K Ishiyama, M Sendoh, and KI Arai, "Magnetic micromachines for medical applications," Journal of Magnetism and Magnetic Materials **242**, 41–46 (2002).

[18] Bradley J Nelson, Ioannis K Kaliakatsos, and Jake J Abbott, "Microrobots for minimally invasive medicine," Annual review of biomedical engineering **12**, 55–85 (2010).

[19] Richard Anthony Lewis Jones, *Soft machines: nanotechnology and life* (Oxford University Press, 2004).

[20] Volker Schaller, Christoph Weber, Christine Semmrich, Erwin Frey, and Andreas R Bausch, "Polar patterns of driven filaments," Nature **467**, 73–77 (2010).

[21] Timothy Sanchez, David Welch, Daniela Nicastro, and Zvonimir Dogic, "Cilia-like beating of active microtubule bundles," Science **333**, 456–459 (2011).

[22] Edward M Purcell, "Life at low reynolds number," Am. J. Phys **45**, 3–11 (1977).

[23] B Abecassis, C Cottin-Bizonne, C Ybert, A Ajdari, and L Bocquet, "Boosting migration of large particles by solute contrasts," Nature materials **7**, 785–789 (2008).

[24] John L Anderson, "Colloid transport by interfacial forces," Annual review of fluid mechanics **21**, 61–99 (1989).

[25] Walter F. Paxton, Kevin C. Kistler, Christine C. Olmeda, Ayusman Sen, Sarah K. St. Angelo, Yanyan Cao, Thomas E. Mallouk, Paul E. Lammert, and Vincent H. Crespi, "Catalytic nanomotors: Autonomous movement of striped nanorods," Journal of the American Chemical Society **126**, 13424–13431 (2004).

[26] Wei Gao, Sirilak Sattayasamitsathit, Jahir Orozco, and Joseph Wang, "Highly efficient catalytic microengines: template electrosynthesis of polyaniline/platinum microtubes," Journal of the American Chemical Society **133**, 11862–11864 (2011).

[27] Apabrita Mallick, Dipti Lai, and Soumyajit Roy, "Autonomous movement induced in chemically powered active soft-oxometalates using dithionite as fuel," New Journal of Chemistry **40**, 1057–1062 (2016).

[28] Wei Wang, Luz Angelica Castro, Mauricio Hoyos, and Thomas E Mallouk, "Autonomous motion of metallic microrods propelled by ultrasound," ACS nano **6**, 6122–6132 (2012).

[29] Ambarish Ghosh and Peer Fischer, "Controlled propulsion of artificial magnetic nanostructured propellers," Nano letters **9**, 2243–2245 (2009).

[30] Rémi Dreyfus, Jean Baudry, Marcus L Roper, Marc Fermigier, Howard A Stone, and Jérôme Bibette, "Microscopic artificial swimmers," Nature **437**, 862–865 (2005).

[31] Stephen J Ebbens and Jonathan R Howse, "In pursuit of propulsion at the nanoscale," Soft Matter **6**, 726–738 (2010).

[32] Joseph Wang and Wei Gao, "Nano/microscale motors: biomedical opportunities and challenges," ACS nano **6**, 5745–5751 (2012).

[33] Wei Wang, Wentao Duan, Suzanne Ahmed, Thomas E Mallouk, and Ayusman Sen, "Small power: Autonomous nano-and micromotors propelled by self-generated gradients," Nano Today **8**, 531–554 (2013).

[34] Jens Elgeti, Roland G Winkler, and Gerhard Gompper, "Physics of microswimmers-single particle motion and collective behavior: a review," Reports on progress in physics **78**, 056601 (2015).

[35] Tim Sanchez, Daniel TN Chen, Stephen J DeCamp, Michael Heymann, and Zvonimir Dogic, "Spontaneous motion in hierarchically assembled active matter," Nature **491**, 431–434 (2012).

[36] Gayathri Jayaraman, Sanoop Ramachandran, Somdeb Ghose, Abhrajit Laskar, M Saad Bhamla, PB Sunil Kumar, and R Adhikari, "Autonomous motility of active filaments due to spontaneous flow-symmetry breaking," Physical review letters **109**, 158302 (2012).

[37] Abhrajit Laskar, Rajeev Singh, Somdeb Ghose, Gayathri Jayaraman, PB Sunil Kumar, and R Adhikari, "Hydrodynamic instabilities provide a generic route to

spontaneous biomimetic oscillations in chemomechanically active filaments," Scientific reports **3** (2013), 10.1038/srep01964.

[38] Abhrajit Laskar and R Adhikari, "Brownian microhydrodynamics of active filaments," Soft matter **11**, 9073–9085 (2015).

[39] Rajesh Singh and R Adhikari, "Traction relations for active colloids and their application," arXiv preprint arXiv:1603.05735 (2016).

[40] R. Singh and R. Adhikari, "Universal hydrodynamic mechanisms for crystallization in active colloidal suspensions," Phys. Rev. Lett. **117**, 228002 (2016).

[41] Rajesh Singh, Somdeb Ghose, and R Adhikari, "Many-body microhydrodynamics of colloidal particles with active boundary layers," Journal of Statistical Mechanics: Theory and Experiment **2015**, P06017 (2015).

[42] "See supplemental material at https://goo.gl/28V9wY for movies of the dynamical states of the colloid-filament assembly.".

[43] Konstantin Klenin and Jörg Langowski, "Computation of writhe in modeling of supercoiled dna," Biopolymers **54**, 307–317 (2000).

[44] M. J. Lighthill, "On the squirming motion of nearly spherical deformable bodies through liquids at very small reynolds numbers," Communications on Pure and Applied Mathematics **5**, 109–118 (1952).

[45] Rolf Erwin Isele-Holder, Julia Jäger, Guglielmo Saggiorato, Jens Elgeti, and Gerhard Gompper, "Dynamics of self-propelled filaments pushing a load," Soft Matter (2016), 10.1039/c6sm01094f.

[46] Walter F Paxton, Ayusman Sen, and Thomas E Mallouk, "Motility of catalytic nanoparticles through self-generated forces," Chemistry–A European Journal **11**, 6462–6470 (2005).

[47] BU Felderhof, "Stokesian spherical swimmers and active particles," Physical Review E **91**, 043018 (2015).

[48] BU Felderhof, "Spinning swimming of volvox by tangential helical wave," arXiv preprint arXiv:1601.00755 (2016).

[49] Chih-kuan Tung, Florencia Ardon, Anubhab Roy, Donald L Koch, Susan S Suarez, and Mingming Wu, "Emergence of upstream swimming via a hydrodynamic transition," Physical review letters **114**, 108102 (2015).

[50] Erik M Gauger, Matthew T Downton, and Holger Stark, "Fluid transport at low reynolds number with magnetically actuated artificial cilia," The European Physical Journal E **28**, 231–242 (2009).